Particle-pore-scale modelling and analysis of heat transfer in packed beds effects of bed porosity and pore structure

Zou, Yi; Kuang, Shibo; Wu, Yongli; Yu, Aibing

DOI
10.1016/j.applthermaleng.2025.127601

Publication date
2025

Document Version
Final published version

Published in
Applied Thermal Engineering

Applied Thermal Engineering 279 (2025) 127601

Contents lists available at ScienceDirect

Applied Thermal Engineering

journal homepage: www.elsevier.com/locate/apthermeng

Research Paper

Particle-pore-scale modelling and analysis of heat transfer in packed beds: effects of bed porosity and pore structure

Yi Zou [a], Shibo Kuang [a,*], Yongli Wu [c], Aibing Yu [b,*]

[a] ARC Research Hub for Smart Process Design and Control, Department of Chemical and Biological Engineering, Monash University, Clayton 3800, Australia
[b] Southeast University, School of Energy and Environment, Nanjing 210096, China
[c] Faculty of Civil Engineering & Geosciences, Delft University of Technology 2628 CN Delft, the Netherlands

ARTICLE INFO

Keywords:
Pore network model
Heat transfer
Packed bed
Bed porosity
Pore structure

ABSTRACT

In packed beds, bed structure significantly influences heat transfer between particles and fluids. A pore-network model (PNM) incorporating conduction, convection, and radiation is developed to investigate heat transfer in packed beds at the particle-pore scale. The model reveals how structural variations, such as bed porosity and pore geometry, influence heat transfer mechanisms. Validation against experimental data from demonstrates strong agreement in temperature evolution and heat transfer coefficients, confirming the model's accuracy. Bed-scale simulations reveal that bed porosity, gas velocity, and temperature collectively determine the dominant heat transfer mode. Convective heat transfer prevails at higher gas velocities, accounting for over 80 %, particularly in loosely packed beds. Conduction is more significant in denser beds and at lower velocities, contributing up to 40 %. Radiative heat transfer becomes substantial, accounting for up to 30 % only at elevated temperatures (e.g., 1000 °C), surpassing conduction in loosely packed configurations. At the pore scale, denser beds exhibit more uniform pore geometries that enhance local convective transfer through pores with near-regular shapes, such as smaller pores approximately half the particle size, typically observed in cells with porosities below 0.4. Conversely, increased heterogeneity in high-porosity beds promotes advective transport through larger pore throats. This model offers convenience in exploring and quantifying how bed porosity and local structural heterogeneity governs heat transport in granular systems and offers a flexible modelling framework for exploring structure–property relationships under diverse thermal and flow conditions.

1. Introduction

Heat transfer during fluid flows through packed beds is crucial for numerous industrial applications, such as blast furnaces, fixed bed reactors, porous-media combustion, and heat/power generation [1–4], where interpore heat transfer plays a central role. This phenomenon involves a complex interplay of conduction, convection, and radiation, greatly influenced by the heterogeneous nature of the inter-particle pore structure. The variability in pore structure primarily dictates the thermal interactions between the fluid and particle phases, affecting the contact area and shape between particle–particle and particle–fluid interactions [5]. Consequently, understanding the structural characteristics of particle beds and their effects on fluid flow and heat transfer is essential for optimizing heat transfer within particulate systems.

Despite the significant experimental [6,7] and theoretical efforts [8,9] in the past decades, comprehensive studies of heat transfer at a pore scale are lacking in understanding the relationship between the packing structure of particle beds and their heat transfer properties. Previous experimental and theoretical analyses of heat transfer introduced various simplifications, for example, treating the bed as a homogeneous entity due to the complex internal structures of porous media and quantifying critical heat transfer properties like effective thermal conductivity based on macroscopic parameters such as bed porosity. Recent advancements in experimental techniques allow for more detailed investigations into pore structures within particle beds [10,11]. However, conducting comprehensive measurements on essential heat transfer properties remains prohibitively expensive and labor-intensive.

Numerical modeling has emerged as a powerful tool for examining the effects of particle bed structure on heat transfer phenomena in particle–fluid systems, offering cost-effectiveness and insights into fluid flow dynamics within beds. Numerical simulations in this area can be categorized based on the computational scale of interest. The primary

* Corresponding authors.
E-mail addresses: shibo.kuang@monash.edu (S. Kuang), yu@simpas.cn (A. Yu).

https://doi.org/10.1016/j.applthermaleng.2025.127601
Received 7 May 2025; Received in revised form 7 July 2025; Accepted 16 July 2025
Available online 18 July 2025

Nomenclature

A_i, A_{ij}	radiation exchange area, m^2
A_{ik}	spherical triangle surface of particle k, m^2
c_p	specific heat transfer of particle, J/(kg·K)
c_f	specific heat transfer of fluid, J/(kg·K)
d_{ij}	distance between particle i and j, m
d_p	particle diameter, m
D_{ij}	effective diameter of pore throat, m
D_{ij}^*	modified effective diameter of pore throat, m
F_{ij}	view factor between particle surfaces
$\mathbf{F}_{d,ij}$	viscous damping force, N
$\mathbf{F}_{c,ij}$	elastic force, N
h_{ik}	convective heat transfer coefficient between particle k and pore i, W/m^2
h_{cond}	heat transfer coefficient by conduction, W/m^2
h_{conv}	heat transfer coefficient by convection, W/m^2
h_{rad}	transfer coefficient by radiation, W/m^2
h_{total}	total transfer coefficient of packed bed, W/m^2
H	gap between particles, m
I_i	moment of inertia, $kg·m^2$
k_c	number of contacts
k_p	thermal conductivity of particles, W/(m·K)
k_f	thermal conductivity of fluid, W/(m·K)
L_{ij}	throat length, m
m_i	particle mass, kg
$\mathbf{M}_{t,ij}$	tangential torque, N·m
$\mathbf{M}_{r,ij}$	rolling torque, N·m
P_i	pore pressure, Pa
Pr	Prandtl number
q_{ij}	volumetric flow rate between pore i and j, m^3/s
$Q_{cond,i}$	heat transfer rate of particle i due to conduction, J/s
$Q_{conv,i}$	heat transfer rate of particle i due to convection, J/s
$Q_{radi,i}$	heat transfer rate of particle i due to radiation, J/s
$Q_{cond1,ij}^{pp}$	particle–fluid-particle conductive heat transfer rate, J/s
$Q_{cond2,ij}^{pp}$	particle–particle conductive heat transfer rate, J/s
$Q_{radi,ij}^{pp}$	particle–particle radiative heat transfer rate, J/s
$Q_{cond,ij}^{ff}$	pore–pore conductive heat transfer rate, J/s
$Q_{conv,ik}^{pf}$	particle-pore convective heat transfer rate, J/s
r_{sf}	determined by Eq. (9), m
r_{ij}	lens of fluid between two spheres, m
r_{sij}	radius of the contact circle between particles i and j, m
r_c	particle–particle contact radius, m
R	particle radius, m
Re_k	Reynold Number of particle k
S_{ij}	contact area between pore i and j, m^2
T_{pi}	temperature of particle i, K
T_{fi}	temperature of pore i, K
U_{ij}	flow velocity between pore i and j, m/s
$\mathbf{v}_i$	translational velocity of particle i, m/s
V_i	volume of pore i, m^3
V_{ij}	volume of Voronoi polyhedra between particles i and j, m^3

Greek Letters

ε_{pi}	emissivity of the sphere i
ϵ	cell porosity
ρ_f	fluid density, kg/m^3
μ	dynamic viscosity, kg/(m·s)
μ_{ij}	advective heat transfer rates between pore i and j, J/s
σ	Stefan-Boltzmann constant, W/m^2K^4
$\boldsymbol{\omega}_i$	angular velocity of particle i, rad/s

category utilizes conventional continuum methods, such as computational fluid dynamics (CFD) [12], which solve Navier-Stokes equations and enable detailed analysis of flow dynamics and thermal properties. Some studies have also coupled CFD models with the discrete element method (DEM) [13,14] to simulate particle–fluid flows and heat transfer at a particle scale. However, such methods, also called unresolved CFD-DEM models [15,16], often overlook the detailed flow and heat transfer around individual particles. Generally, previous CFD and CFD-DEM methods fail to capture detailed pore structures, limiting their ability to depict local fluid flow and heat transfer around particles.

The second category includes methods that can operate at the sub-particle scale [17,18]. These approaches, also called resolved models, provide detailed and accurate depictions of fluid flow at the pore space around particles, enabling investigations into fluid velocity distributions and the impact of bed structures on local fluid dynamics and heat transfer properties. However, the computational demands of these methods are significant, often limiting their application to small-scale, laboratory-based studies.

In this context, developing an approach that simulates fluid flows and heat transfer in particle beds at a comparable or intermediate scale is beneficial while providing a detailed depiction of the pore structure. Compared to unresolved CFD, the pore network model (PNM) [19,20] effectively represents the essential structural features and computes fluid flows and heat transfer at the pore scale within particle assemblies. Typically, these pore structures are characterized based on the Delaunay tessellation of particle centers. Fluid flow conductance is calculated by considering the cross-sectional area and length of the pore structures. At the same time, particle–fluid heat transfer is assessed by considering the contact area within the pore structure. This topological framework adeptly captures critical aspects of porous media, such as heterogeneity and interconnectivity, offering comprehensive and relevant insights.

Significant advancements have been achieved in the development of the PNM since Fatt's work [21]. The accuracy in representing pore geometry has notably improved, and the method has been applied to various applications, as detailed in Blunt's review [22]. Among these studies, considerable emphasis has been placed on elucidating the interplay between pore structures, flow properties, and heat transfer within particle beds. For example, Tomac and Gutierrez [23] introduced a 2D convective-conductive heat transfer model using the DEM, incorporating a pipe network approach proposed by Cheng et al. [24]. Similarly, Chen et al. [25] simulated heat and mass transfer within particle packings using a 2D PNM. Cheng et al. [26] expanded this methodology for 3D analyses by applying Delaunay tessellation and explored heat transfer across fluid voids and the impact of packing structures. Caulk et al. [27] adopted a pore-scale numerical strategy to model heat transfer and its thermo-hydro-mechanical interactions in granular media, integrating DEM with the Finite Volume Method (FVM) for comprehensively assessing conductive and advective heat transfer. Additionally, Morimoto et al. [28] proposed a novel formula for the Nusselt number in thermo-hydro-mechanical analyses by combining DEM with a PNM.

While advancements have been made, current research still exhibits certain limitations. For example, some studies are limited to 2D models [23,25], which restricts the applicability of such studies to real-world scenarios where 3D pore structures are often critical. Also, many existing studies only focused on specific aspects of heat transfer using simplified models. For example, some studies ignored the advective and convective heat transfer due to pore-scale fluid flow [24,26], while others failed to incorporate radiative heat transfer at a pore-scale level [27,28]. To date, comprehensive heat transfer models that integrate all

major heat transfer mechanisms in particulate-fluid systems are rarely reported in the literature. Achieving a thorough understanding of heat transfer remains elusive without fully incorporating all the primary heat transfer mechanisms. Moreover, existing studies often overlooked localized variations in pore structures and their impact on heat transfer despite these localized variations significantly influencing the overall heat transfer characteristics. Although recent research has begun to explore local-scale variability in packed beds [29,30], these efforts have primarily focused on the effects of local structure on effective thermal conductivity. Comprehensive and general studies addressing the influence of local pore structures on particle–fluid heat transfer remain scarce.

This work presents a novel modelling framework that integrates all major heat transfer mechanisms at the particle–pore scale, enabling detailed quantification of the porosity-dependent contributions to overall heat transfer. Additionally, it introduces a microscopic approach to assess the influence of pore geometry on local heat transfer behaviour. The structure of this paper is organized as follows: First, a detailed description of the model is presented, followed by model validation. The model is then applied to elucidate the interconnections between heat transfer mechanisms and bed/pore structures. Finally, the key findings of the study are summarized.

2. Model description

2.1. Model framework

The model framework is illustrated in Fig. 1. Initially, particle packings are generated using a DEM model. Based on the results, Voronoi tessellation is then applied to create the particle connection model, while Delaunay tessellation is used to develop the pore network model. The particle connection model simulates particle–particle conductive and radiative heat transfer, as detailed by Cheng [24,31]. Meanwhile, the pore network model simulates particle-pore convective, pore–pore conductive, and advective heat transfer.

2.2. DEM model

In the DEM originally developed by Cundall and Strack [32], the governing equations for translational and rotational movements of particle i are described by [14,33]:

$$m_i\frac{d\mathbf{v}_i}{dt}=\sum_{j=1}^{k_c}\left(\mathbf{F}_{c,ij}+\mathbf{F}_{d,ij}\right)+m_i\mathbf{g} \tag{1}$$

$$I_i\frac{d\omega_i}{dt}=\sum_{j=1}^{k_c}\left(\mathbf{M}_{t,ij}+\mathbf{M}_{r,ij}\right) \tag{2}$$

where m_i is the particle mass, I_i is the moment of inertia, and $\mathbf{v}_i$ and $\boldsymbol{\omega}_i$ represent the translational and angular velocities of, respectively, with k_c denoting the count of particles interacting with it. The forces acting on a particle include the gravitational force $m_i\mathbf{g}$, and particle–particle/wall interaction forces. The latter encompasses the elastic force $\mathbf{F}_{c,ij}$ and the viscous damping force $\mathbf{F}_{d,ij}$, both of which can be decomposed into normal and tangential components. The torque on particle i due to its interaction with particle j comprises two elements: $\mathbf{M}_{t,ij}$, resulting from the tangential force, and $\mathbf{M}_{r,ij}$, known as the rolling friction torque. The latter arises from the elastic hysteresis loss and viscous dissipation associated with particle–particle/wall contacts, mitigating the relative rotation between particles. Given that a particle can engage in multiple interactions, the sum of all individual interaction forces and torques over the k_c particles in contact with particle i is considered.

2.3. Pore network flow model

In the pore network model, fluid flow's mass and momentum balances are applied to individual pore units. Each pore unit is represented by a tetrahedron derived from Delaunay tessellation. Fig. 2 illustrates a pore unit and its connectivity to adjacent pores, where the tetrahedron's four vertices correspond to the centers of four spheres, defining the pore space at their interstice. Additionally, each tetrahedron face features a free area (S_{ij}), unoccupied by the particles, facilitating the fluid flow between two neighboring pores through these areas. The conduit for this flow, known as the pore throat, is modeled as a cylindrical tube connecting the centers of adjacent pores, with its effective diameter (D_{ij}) specified by: $D_{ij}=\sqrt{4S_{ij}/\pi}$. Another critical parameter, the throat length (L_{ij}), measures the distance between the centers of two neighboring pores. This parameter is instrumental in deriving the relationship between fluid flow and pressure difference across the pores, following a modified Hagen-Poiseuille equation [34]:

$$P_i-P_j=\frac{32\mu L_{ij}}{D_{ij}^{*2}}U_{ij}+\frac{\rho_f L_{ij}}{2D_{ij}^{*}}U_{ij}^{2} \tag{3}$$

where P_i and P_j are the pressure of pore i and pore j, respectively, μ is the dynamic viscosity, ρ_f is the fluid density, U_{ij} is the flow velocity between pore i and pore j, D_{ij} is modified as D_{ij}^{*} by a shape factor [20].

Furthermore, mass balance equations are established for each pore unit, expressed as:

$$\sum_{j=1}^{4}q_{ij}=\sum_{1}^{4}\int_{S_{ij}}(\mathbf{u}-\mathbf{v})\bullet nds=-\frac{\partial V_i}{\partial t}=0 \tag{4}$$

where q_{ij} is the volumetric flow rate between pore i and j, $\mathbf{u}$ and $\mathbf{v}$ are the velocities of the fluid and particle, respectively. $\mathbf{n}$ is the local normal

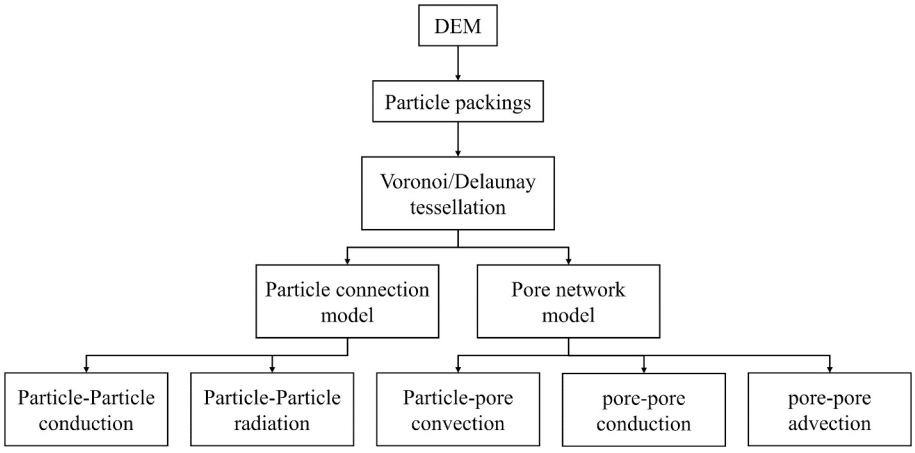

Fig. 1. Model framework of the current particle-pore scale heat transfer model.

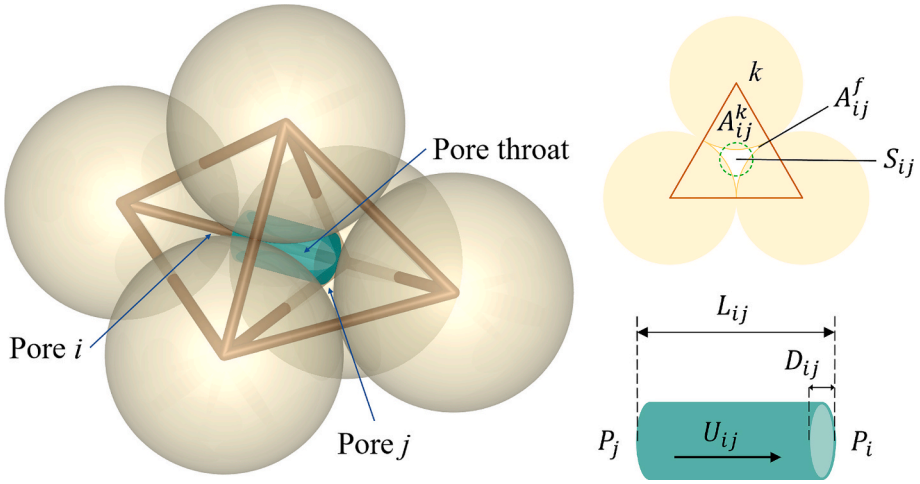

Fig. 2. Schematic illustration of a typical pair of pore units and the pore throat between pore *i* and pore *j*.

vector of S_{ij}, V_i is the volume of the pore unit *i*, and $\partial V_i/\partial t$ is the rate of change in pore volume over time, which is zero in a packed bed.

2.4. Heat transfer model

The governing equation of heat transfer for particle *i* is expressed as:

$$m_i c_p \frac{dT_{pi}}{dt} = Q_{cond,i} + Q_{conv,i} + Q_{radi,i} \tag{5}$$

where $Q_{cond,i}$, $Q_{conv,i}$ and $Q_{radi,i}$ denote the sum of heat exchange rates for particle *i* due to convection, conduction, and radiation, respectively, T_{pi} is the temperature of particle *i*, and c_p represents the specific heat of the particle at constant pressure.

Assuming that each pore is an open thermodynamic system, the energy balance of pore *i* can be written as:

$$\frac{dT_{fi}}{dt} = \frac{\sum_{j=1}^{4}\left(\mu_{ij} + Q_{cond,ij}^{ff}\right) + \sum_{k=1}^{4} Q_{conv,ik}^{pf}}{c_f \rho_f V_i} \tag{6}$$

where μ_{ij}, $Q_{cond,ij}^{ff}$ and $Q_{conv,ik}^{pf}$ denote the heat exchange rates due to pore–pore advection, pore–pore conduction, and particle-pore convection, respectively. T_{fi} is the temperature of pore *i*, c_f is the fluid's heat capacity, ρ_f is the fluid density, and V_i is the pore volume. The heat exchange rates associated with different heat transfer mechanisms in Eqs (5) and (6) are given as follows:

2.4.1. Particle-particle conductive heat transfer

Conduction heat transfer between particles in a packed bed encompasses two key mechanisms: (1) non-contact conduction through the fluid between particles and (2) direct conduction through static contact between particles, as depicted in Fig. 3(a). The modeling approach for these mechanisms is elaborated below.

For modeling particle–fluid-particle heat transfer, the model proposed by Cheng [24] is adopted. This model quantifies the heat transfer rate between two spheres *i* and *j* by

$$Q_{cond1,ij}^{pp} = (T_{pi} - T_{pj}) \times \int_{r_{sij}}^{r_{sf}} \frac{2\pi \bullet r dr}{\left(\sqrt{R^2 - r^2} - r(R+H)/r_{ij}\right) \bullet (1/k_{pi} + 1/k_{pj}) + 2\left[(R+H) - \sqrt{R^2 - r^2}\right]/k_f} \tag{7}$$

where

$$H = (d_{ij} - 2R)/2 \tag{8}$$

$$r_{sf} = \frac{R \bullet r_{ij}}{\sqrt{r_{ij}^2 + (R+H)^2}} \tag{9}$$

$$r_{ij} = \sqrt{3V_{ij}/(\pi \bullet d_{ij})} \tag{10}$$

In these equations, k_{pi} and k_{pj} represent the thermal conductivities of particles *i* and *j*, respectively. The parameter r_{sij} is defined based on the gap *H* between particles, equaling 0 for $H \geq 0$ (i.e., no contact) and r_c when $H < 0$ (i.e., direct contact). V_{ij} is the volume of Voronoi polyhedra between particles *i* and *j*. The radius r_{ij} corresponds to the lens of fluid between two spheres, whether in contact or near contact. Following the work of Zhou [35], the heat transfer is considered negligible when the ratio of the gap *H* to the radius *R* reaches 0.5, indicating the distance at which the thermal influence of one particle on another becomes minimal.

For the heat conduction through particle–particle static contact, the model proposed by Batchelor and O'Brien [36] is employed to calculate the heat transfer rate $Q_{cond2,ij}^{pp}$ across the contact area between particles *i* and *j*:

$$Q_{cond2,ij}^{pp} = \frac{4r_c(T_{pj} - T_{pi})}{(1/k_{pi} + 1/k_{pj})} \tag{11}$$

2.4.2. Particle-particle radiative heat transfer

In many previous studies [37,38], the radiative heat transfer for each particle is modeled by considering an isolated domain as its environment. Within this specified enclosed cell (often assumed to be 1.5 d_p in the literatures), an environmental temperature is assumed to represent the enclosed surface temperature surrounding the particle. The equation

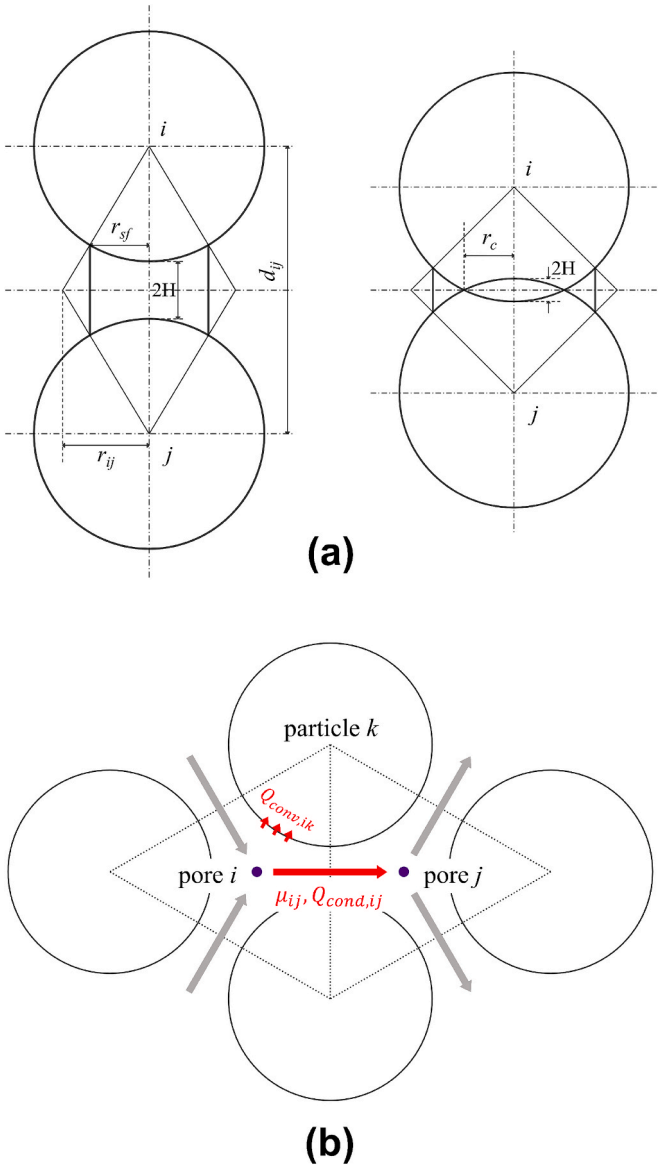

Fig. 3. Illustration of heat transfer mechanisms: (a) particle–particle and (b) particle-pore and pore–pore.

is written as follows:

$$Q_{rad,i} = \sigma \varepsilon_{pi} A_i \left({T_{local,i}}^4 - T_i^4 \right) \tag{12}$$

where $T_{local,i}$ is the average temperature of particles and fluid by volume fraction within an enclosed spherical domain, T_i is the temperature of particle i. A_i is the radiative exchange area of particle i, which is its surface area in this case. σ represents the Stefan-Boltzmann constant, a fundamental physical constant in thermodynamics dictating the amount of radiant energy emitted per unit area of a black body per unit time and temperature, valued at 5.67E-08 W/(m^2·K^4). The emissivity of the sphere ε_{pi} characterizes the efficiency of the spheres as radiators, set to 0.8 for this study. This approach simplifies the calculation of particle–particle radiation heat transfer by assuming a local environmental temperature; however, it overlooks the impact of the packing structure on the radiative heat transfer of a particle.

On the other hand, Cheng's network method [31] offers a precise framework for quantifying the radiative exchange rate between two uniform spheres and is thus adopted:

$$Q_{radi,ij}^{pp} = \frac{\sigma \left({T_{pi}}^4 - {T_{pj}}^4 \right)}{2\dfrac{\left(1-\varepsilon_{pi}\right)}{\varepsilon_{pi} A_i} + \dfrac{A_{ij}\left(1-F_{ij}\right)}{2}} \tag{13}$$

The radiative exchange area term A_{ij} is determined by the geometric configuration of particles i and j, which can be inferred from the packing structure. F_{ij} accounts for a fraction of radiation leaving surface i that directly reaches surface j, and it is calculated using an extended numerical method provided by Jones [39]. A comparison of the two radiation models will be provided later.

2.4.3. Pore-pore advective heat transfer

As indicated in Fig. 3(b), when fluid flows from pore i to its neighboring pore j, a mass-energy advective heat transfer rate μ_{ij} due to mass-energy flux is used to represent the energy carried by the fluid, calculated by

$$\mu_{ij} = \begin{cases} q_{ij} c_f \rho_f T_{fi} & q_{ij} > 0 \\ q_{ij} c_f \rho_f T_{fj} & q_{ij} < 0 \end{cases} \tag{14}$$

where T_{fi} and T_{fj} represent the temperatures of pores i and j, respectively, and q_{ij} is the volumetric flow rate of the fluid flow, c_f is the fluid specific heat capacity.

2.4.4. Pore-pore conductive heat transfer

The pore–pore conductive heat transfer occurs through the common interfaces between adjacent pores, calculated by

$$Q_{cond,ij}^{ff} = \frac{k_f S_{ij}}{L_{ij}} \left(T_{fi} - T_{fj} \right) \tag{15}$$

where k_f is the fluid thermal conductivity, S_{ij} and L_{ij} are the contact area of two pores and throat length, respectively.

2.4.5. Particle-pore convection

The convective heat transfer rate between particle k and pore i is expressed as

$$Q_{conv,ik}^{pf} = h_{ik} A_{ik} \left(T_{pk} - T_{fi} \right) \tag{16}$$

where A_{ik} is the spherical triangle surface of particle k interacting with the pore i, T_{fi} is the temperature of the pore i, T_{pk} is the temperature of particle k, and h_{ik} is the convective heat transfer coefficient. h_{ik} is associated with the Nusselt number, which can be empirically estimated based on local cell porosity and Reynolds number, as proposed by Gunn et al [40]:

$$Nu_{ik} = \begin{array}{l} \left(7 - 10\epsilon + 5\epsilon^2\right)\left(1 + 0.7 {\mathrm{Re}_k}^{0.2} \mathrm{Pr}^{1/3}\right. \\ \left. + \left(1.33 - 2.4\epsilon + 1.2\epsilon^2\right) {\mathrm{Re}_k}^{0.7} \mathrm{Pr}^{1/3}\right) \end{array} \tag{17}$$

where Re_k is the local relative Reynolds number for particle k. ϵ is the cell porosity for pore i. The fluid Prandtl number Pr is a material property. For simplicity, it is assumed to be a constant in this work, set to 0.712.

2.5. Numerical solution and conditions

As shown in Fig. 4, the packed beds considered are configured with dimensions of $16d_p \times 16d_p \times 16d_p$, where d_p represents the particle diameter set at 1 mm. In the DEM simulations, beds with varying global porosities were generated by adjusting the inter-particle friction coefficient. During the packing process, particles were allowed to settle under gravity via free fall. Periodic boundary conditions are applied to highlight the effects of pore structure and eliminate wall effect. The resulting packings exhibit a range of porosities between 0.428 and 0.698, facilitating an analysis of how the structural composition of the bed influences its thermal properties. Within these simulations, the spheres constituting the packed beds are stationary. The simulations are

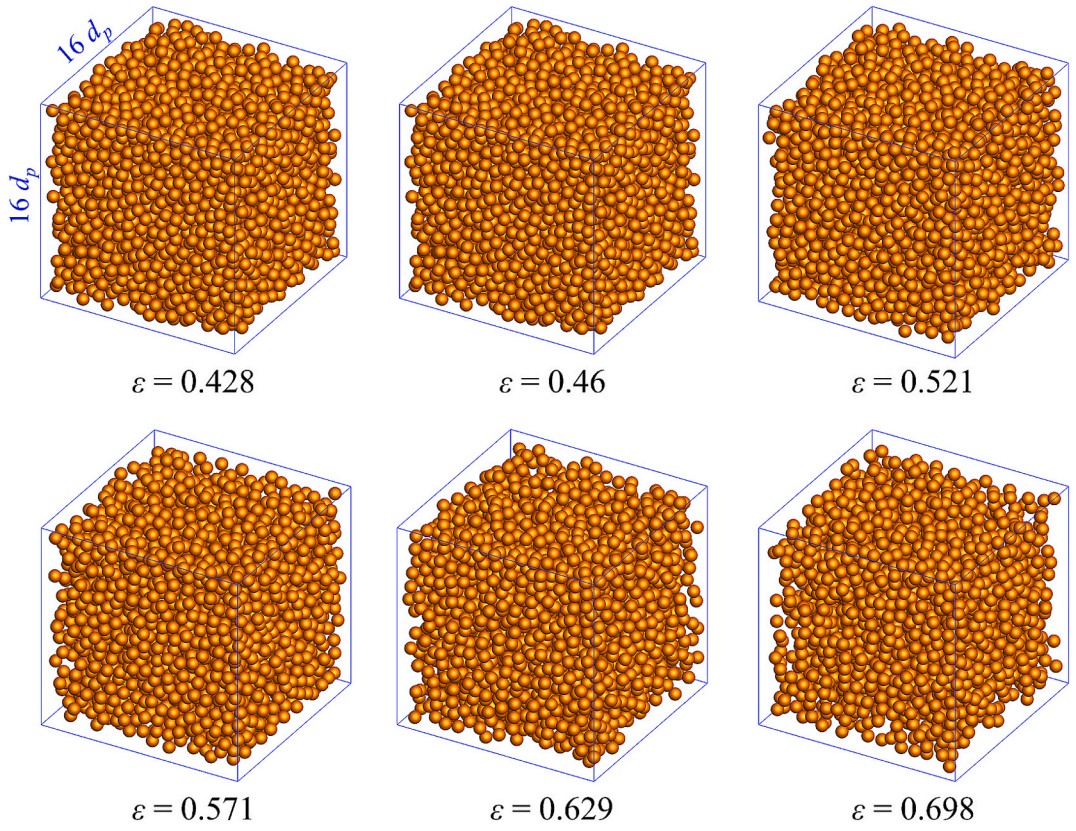

Fig. 4. Particle beds with varying porosities used in the simulation to study the effects of bed structure on thermal behavior.

Table 1
Parameters used in the present simulations.

Simulation parameters	Values
Diameter of bed particles d_p	3 mm, 1 mm
Diameter of hot spheres d_p	3 mm, 2 mm
Density of bed particles ρ_p	420 kg/m^3
Density of hot spheres ρ_p	8,850 kg/m^3
Thermal conductivity of bed particles k_p	0.84 W/(m·K)
Thermal conductivity of hot spheres k_p	55 W/(m·K)
Specific heat capacity of bed particles c_p	800 J/(kg·K)
Specific heat capacity of hot spheres c_p	351 J/(kg·K)
Initial temperature of bed particles	25 °C
Initial temperature of hot spheres	180 °C
Particle-particle/wall sliding friction μ_s	0.2, 0.5, 1.4, 2.6, 3.8, 5.0
Particle-particle/wall rolling friction μ_r	0.003, 0.05, 0.14, 0.26, 0.38, 0.5
Particle Young's modulus E	5.0×10^9 kg/(m·s^2)
Particle Poisson ratio ν	0.3
Time step Δt	1.75×10^{-6} s
Fluid temperature T_f	25 °C
Fluid density ρ_f	1.205
Fluid molecular viscosity μ_f	1.8×10^{-5} Pa·s
Fluid thermal conductivity k_f	$2.873 \times 10^{-2} + 7.76 \times 10^{-5} T_f$ W/(m·K)
Fluid specific heat capacity c_f	$1002.737 + 1.2324 \times 10^{-2} T_f$ J/(kg·K)
Fluid Prandtl number (Pr)	0.712

designed to apply variable pressures at the top (low pressure) and the bottom (high pressure) of the packed bed, thereby establishing a pressure gradient along the bed's vertical direction. This pressure differential enables the fluid to infiltrate the bed from its base, allowing a comprehensive examination of the thermal behaviors exhibited by all particles within the bed. Initially, the bed is maintained at a room temperature of 25 °C before being subjected to heating by hot gas with different inlet velocities and temperatures. Throughout this heating phase, the thermal responses of all particles are monitored and analyzed across packed beds with varying degrees of porosity. Table 1 lists the simulation parameters used in this study.

Under the conditions given above, the governing equations of fluid flow (Eqs. (3) and (4)) are solved through a well-documented PNM method (see, e.g., the work of Wu et al. [41]). PNM formulates a set of nonlinear equations that characterize fluid velocity and pressure, which

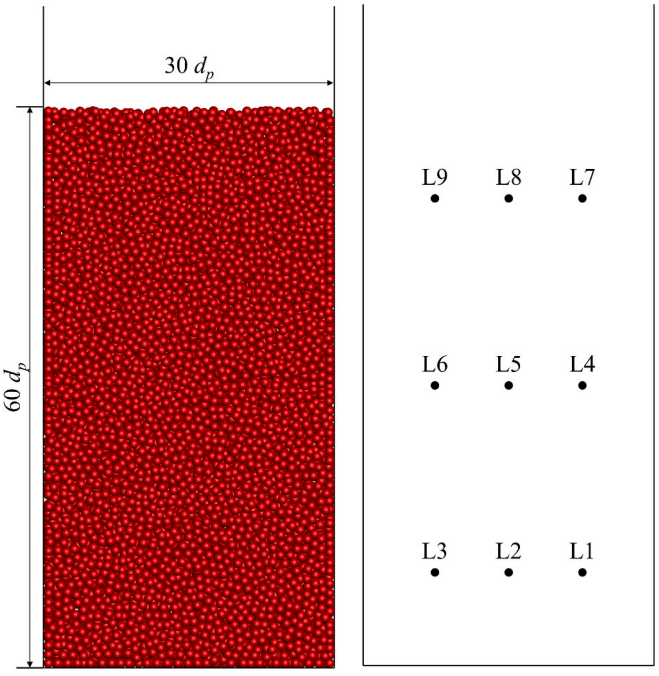

Fig. 5. Simulation setup for cooling of hot spheres: (left) particle bed used in the simulation; (right) initial locations of hot spheres.

can be adeptly solved using algorithms like Gauss-Seidel or advanced solvers such as MKL PARDISO. This PNM framework is extended to consider heat transfer by solving Eqs (7)-(15), accounting for the heat transfer rates between particle–particle, particle-pore, and pore–pore after solving the fluid flow.

2.6. Model validation

2.6.1. Cooling of hot bronze sphere: comparison with experiment

Model validation is necessary before model application. The PNM for simulating flows has been examined previously [42]. The present validation focuses on the simulation of heat transfer. Fig. 5 shows the pseudo-2D "slot" packed bed considered in this study. In order to best simulate the bed used in experiment, the bed in simulation has a thickness of eight particle diameters and a width of thirty particle diameters, filled with 3-mm particles. As previously done [43,44], periodic boundary conditions are applied to the front and back sides to alleviate the computational load. In contrast, wall boundary conditions are taken on the right and left sides. It should be noted that in PNM modeling, the rigid walls is represented by an "infinite-sized" sphere [41]. The wall properties are the same as those for bed particles. The simulation is conducted under a specific scenario: the cooling of hot spheres (initially at 180 °C) immersed in a bed of particles and exposed to room-temperature gas induced from the bottom of the bed, with superficial velocity 0.429 m/s. This setup facilitates the examination of the cooling dynamics of the hot spheres within a constrained environment. The thermal properties of the hot spheres also follow the experiment conducted by Collier [45] for model validation. Correspondingly, a bronze sphere's temperature variations during the cooling process are recorded. Additionally, the impact of the initial positions of the hot spheres is investigated. As depicted on the right side of Fig. 5, each position (L1 to L9) corresponds to a hot sphere.

Fig. 6(a) compares the predicted temperatures with the experimental measurements during the cooling process. The cooling curves for nine hot spheres at different locations within the packed bed (labeled L1 to L9 in Fig. 4) all agree with the experiment data. Fig. 6(b) presents a comparative analysis of the natural logarithm of the temperature difference ratio $\ln[(T_0 - T_b)/(T - T_b)]$ over time. The derived heat transfer coefficients for L1 to L9, ranging from 135.51 to 165.76 W/(m^{2}K), specifically, closely matching the experimental values reported as 145 $\pm$ 15 W/(m^{2}K). The predicted cooling behaviour and heat transfer coefficients agree well with the experimental data by Collier et al. [45] and the simulation trends reported by Zhou et al. [35], affirming the PNM model's applicability in simulating heat transfer phenomena. Additionally, the near-linear trends in Fig. 6(b) suggest a minimal contribution from radiative heat transfer, likely due to the moderate temperatures (≤180 °C) of the bronze spheres, a conclusion in line with the experimental observations.

2.6.2. Comparison of radiation models

To compare the previous radiation model (Eq. (12), referred to as Model A) with the current radiation model (Eq. (13), referred to as Model B), the same packed bed configuration as shown in Fig. 5 is used to simulate the cooling of a single 3 mm hot sphere located at the center of the bed with different initial temperatures. The temperature evolutions of the central sphere during cooling and the radiative heat transfer coefficients of the particle bed are compared for both models.

Fig. 7 shows the cooling curves for a hot sphere at different initial temperatures, located at the center of the packed bed, under a low gas flow rate of 0.2 m/s, using both radiation models. At lower temperatures, such as 180 °C, the cooling curves for both models display nearly identical trends. However, as the temperature increases and the effects of radiation become more pronounced, the differences between the local average approach (Model A) and the particle-pore scale approach (Model B) become more evident in the temperature curves.

To further investigate the cause of these differences, Fig. 8 compares the distributions of the dimensionless radiative heat transfer coefficients h_{rad}* between densely packed and loosely packed beds. The particles' temperatures are all set at room temperature to exclude the effects of temperature. In the traditional radiation model (Model A), due to the averaging of local temperatures, the distribution of radiative heat transfer coefficients shows no distinction between dense and loose beds, indicating that Model A overlooks the impact of bed structure on radiative heat transfer. In contrast, Model B reveals more uniform radiative heat transfer coefficients in densely packed beds, while in loosely packed beds, the coefficients are uneven, with lower values around the pores. This demonstrates that Model B more accurately captures the effects of packing structure on radiative heat transfer, making it the preferred model in this study.

3. Results and discussion

3.1. Overall heat transfer characteristics

This section focuses on the interplay between bed porosity and the averaged thermal attributes of all particles within a packed bed under various conditions. Fig. 9 illustrates the temporal progression of the average bed temperature for packed beds of differing porosity levels, subjected to various gas velocities, with the gas temperature maintained at 100 °C. The average bed temperature is defined as the arithmetic mean of the temperatures of all particles. Packed beds with the same total volume but different porosities contain different numbers of particles, resulting in varying total heat capacities. To isolate the effect of

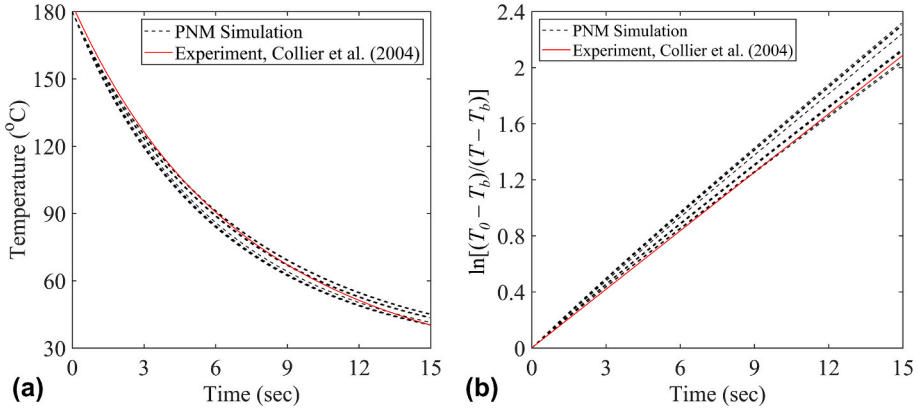

Fig. 6. Comparison between numerical results and experiment data for: (a) Temperature evolution of 2 mm diameter hot spheres; (b) natural logarithm of the temperature difference ratio $\ln[(T_0 - T_b)/(T - T_b)]$ versus time at a gas superficial velocity of 0.429 m/s.

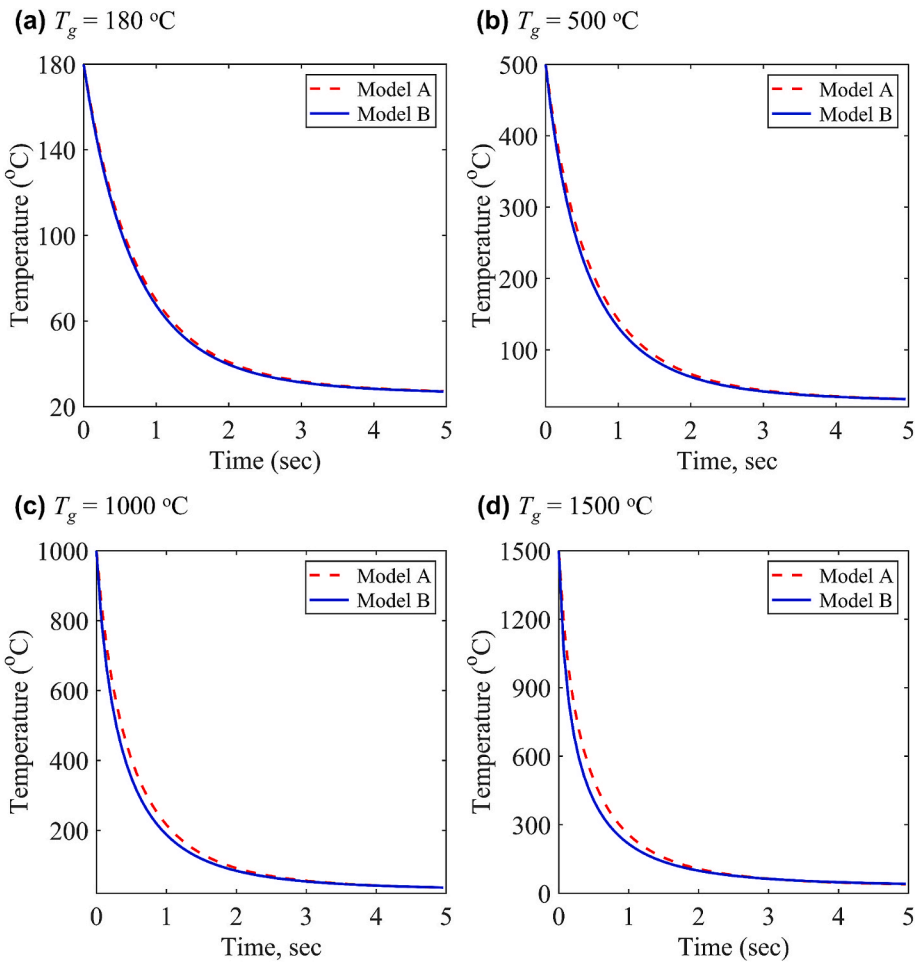

Fig. 7. Temperature evolution comparison between radiation model A and model B during the cooling of a 3 mm hot sphere for a gas velocity of 0.2 m/s at four different gas temperatures: (a) 180 °C, (b) 500 °C, (c) 1000 °C, (d) 1500 °C.

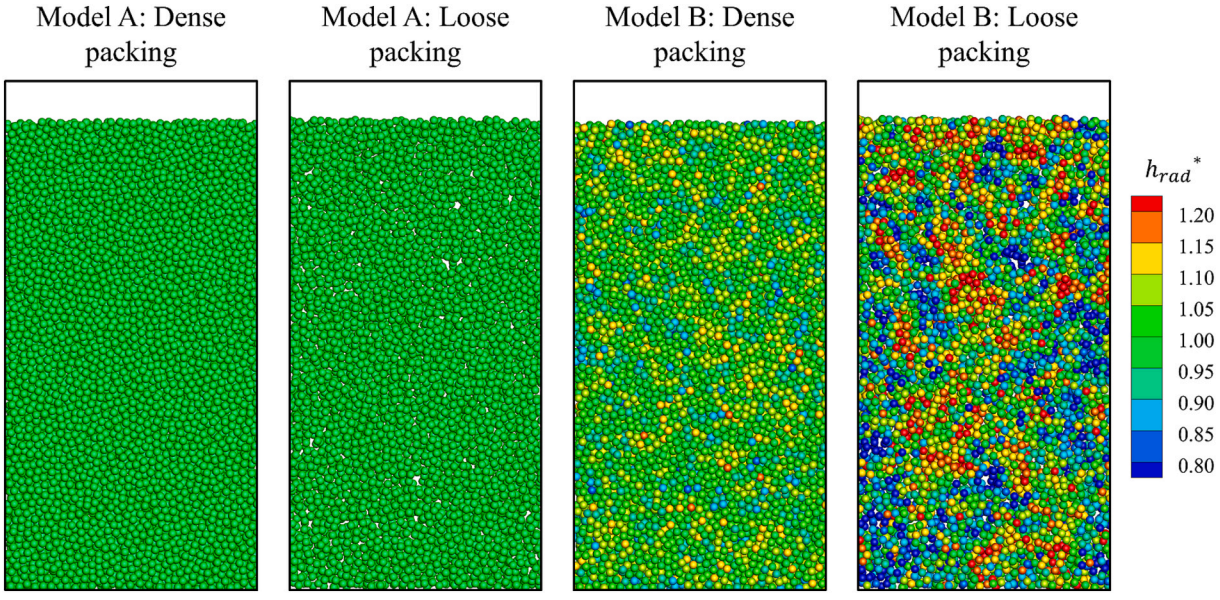

Fig. 8. Comparison of distributions of dimensionless radiative heat transfer coefficients h_{rad}^* between dense and loose particle bed for two different radiation model.

structural differences, it is necessary to eliminate the influence of these variations in heat capacity. Since all particles are identical in material and size, the total heat capacity of the bed is directly proportional to the number of particles. Accordingly, a normalized time τ is introduced to account for differences in total heat capacity across cases, and is defined as: $\tau = t \bullet N_i/N_{0.428}$, where N_i is the number of particles in the current

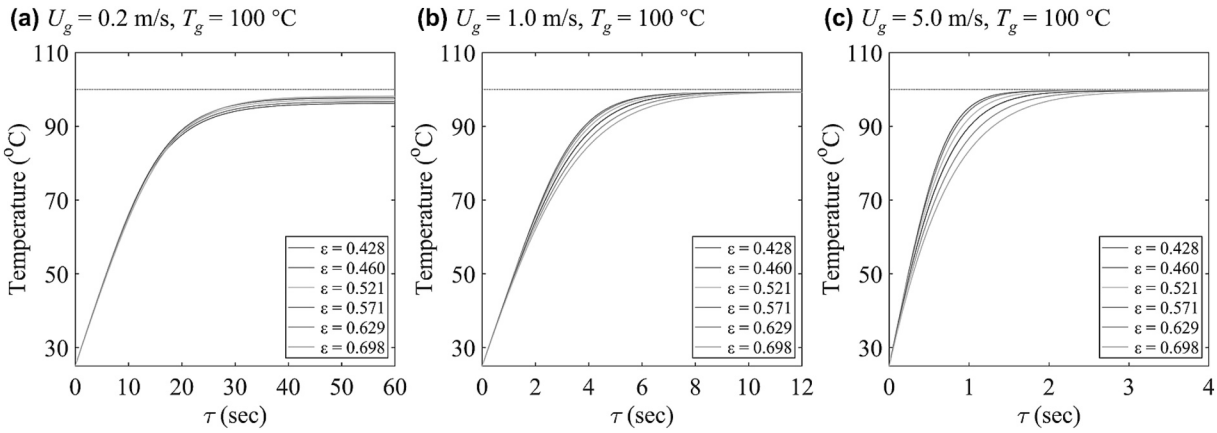

Fig. 9. Average bed temperature over normalized time τ at a gas temperature of 100 °C for gas velocities of (a) 0.2 m/s, (b) 1.0 m/s, and (c) 5.0 m/s.

case, and $N_{0.428}$ is the number of particles in the densest case (ε = 0.428). The normalized time τ can be interpreted as the equivalent time required to heat the current bed if it had the same total heat capacity as the densest bed.

It is observed that an increase in gas velocity significantly reduces the time required for the particles to achieve thermal equilibrium. This observation underscores hot gas velocity's significant role in facilitating the particles' heating process. Furthermore, at higher gas velocities, packed beds with lower porosity exhibit a faster heating rate and reach thermal equilibrium more quickly (Fig. 9(c)). In contrast, at lower gas velocities, the heating rates across beds with different porosities show no significant differences (Fig. 9(a)). This behaviour could be attributed to the fact that, under the same superficial gas velocity, denser beds have smaller void fractions, resulting in higher pore (interstitial) gas velocities. In addition, lower porosity beds possess a higher specific interfacial area, which further facilitates heat exchange between the gas and particles. This leads to an increased convective heat transfer coefficient, thereby enhancing heat transfer to the solid phase. As a result, the effect is more pronounced at higher superficial gas velocity, where convective heat transfer dominates.

Fig. 10 illustrates the evolution of the average bed temperature over time for packed beds with varying porosity levels, subjected to different gas temperatures while maintaining a constant gas velocity of 1.0 m/s. The data indicates that variations in gas temperature exert minimal impact on the duration required for heating the particles to reach thermal equilibrium. However, variations in gas temperature can also influence the heating behaviour of beds with different porosities. Although denser beds generally exhibit higher heating rates due to enhanced convective heat transfer, this advantage diminishes as the gas temperature increases. According to Eq. (13), radiative heat flux scales with the fourth power of temperature. Consequently, at relatively high temperatures, radiation becomes a significant mode of heat transfer, rapidly increasing in contribution and effectively overshadowing the porosity-dependent differences in convective heat transfer.

Fig. 11 plots the percentages of the contributions by different heat transfer mechanisms to overall heat transfer versus bed porosity at a gas temperature of 100 °C for gas velocities of 0.2 m/s, 1.0 m/s, and 5.0 m/s. Each contribution is expressed as the ratio of the effective heat transfer coefficient of the respective mechanism to the total effective heat transfer coefficient of the particles: i.e., h_{cond}/h_{total}, h_{conv}/h_{total}, h_{rad}/h_{total}, representing contributions of conduction, convection, and radiation, respectively. At lower gas velocities, such as 0.2 m/s, particle–particle conduction contributes significantly to the overall heat transfer in low-porosity beds, accounting for over 40 %, second only to particle–fluid convection. As porosity increases, the contribution of conduction decreases slightly, while particle–fluid convection through the pore space becomes increasingly dominant. This trend suggests that, at low gas velocities, increasing bed porosity has a more pronounced negative impact on conduction than on convection. In contrast, at higher gas velocities, such as 5.0 m/s, particle–fluid convection emerges as the overwhelmingly dominant heat transfer mechanism, contributing over 80 % in low-porosity beds and far exceeding the contribution from conduction. Interestingly, with increasing porosity, the contribution of convection shows a slight decline, indicating that at higher velocities, the influence of bed porosity on convective heat transfer becomes slightly more significant than on conductive heat transfer. Moreover, due to the minimal radiative emission of particles within the present temperature range, the contribution of radiative heat transfer between

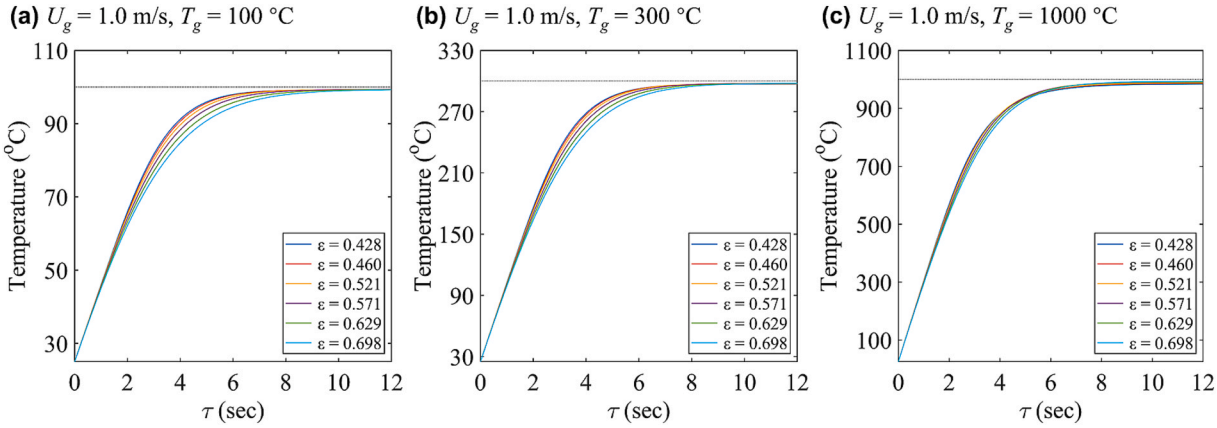

Fig. 10. Average bed temperature over normalized time τ for a gas velocity of 1.0 m/s at a gas temperature of (a) 100 °C, (b) 300 °C, and (c) 1000 °C.

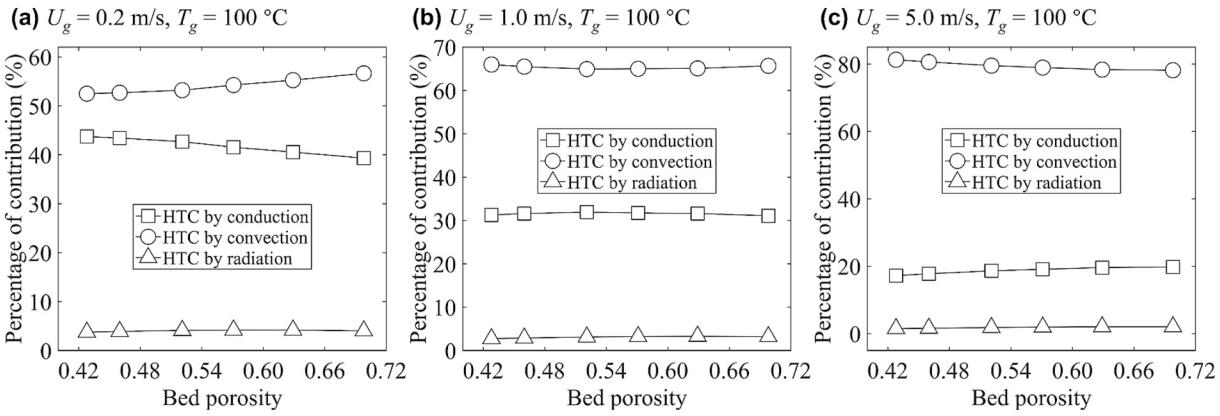

Fig. 11. Contributions of different heat transfer mechanisms as a function of porosity at a gas temperature of 100 °C when U_g = (a) 0.2 m/s, (b) 1.0 m/s, and (c) 5.0 m/s.

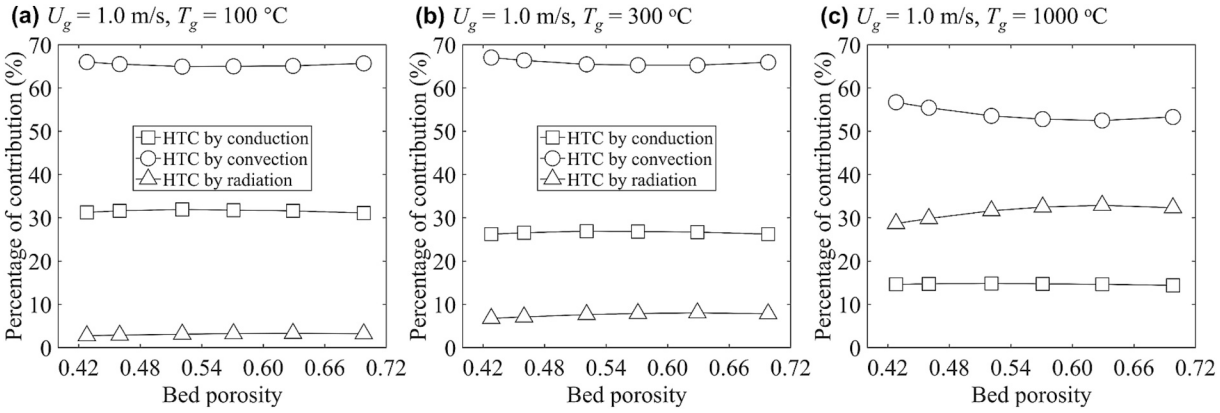

Fig. 12. Contributions of different heat transfer mechanisms as a function of porosity at a gas velocity of 1.0 m/s when T_g = (a) 100 °C, (b) 500 °C, and (c) 1000 °C.

particles remains consistently low across varying bed porosities and decreases further at higher gas velocities.

Fig. 12 shows the influence of gas velocity on the contributions of different heat transfer mechanisms to the overall process at a constant gas velocity of 1.0 m/s. The results reveal that the impact of radiative heat transfer on the overall heat transfer is minimal at lower temperatures. However, as the gas temperature increases, the significance of radiative heat transfer also increases. For instance, at a gas temperature of 300 °C, radiative heat transfer accounts for less than 10 % of the total heat transfer. At significantly higher temperatures, such as 1000 °C, the radiative contribution rises significantly, exceeding 30 % in the loosest packed beds, making it the second most significant mechanism after convection, while the contribution from conduction drops to approximately 15 %. Moreover, an increase in bed porosity leads to a slight increase in the contribution from radiation, attributed to the reduced contribution of convection caused by loose pore structure. These findings indicate that in the cases of high temperature and relatively low gas velocity, radiative heat transfer would become a considerable factor in the particle–fluid heat exchange within a packed bed.

3.2. Pore-scale heat transfer characteristics

The current study simulates fluid flow and heat transfer based on the pore structure within the packed beds. Fig. 13 shows two representative pore structures in packed beds at two different porosities. In the figure, each 'pipe' illustrates the linkage between two pores, with the pipe's thickness symbolizing the normalized throat diameter, quantified as the ratio of the individual throat diameter (D_{ij}) to the mean throat diameter across the system ($<D_{ij}>$). Similarly, the pipe's length represents the normalized throat length, represented by $L_{ij}/<L_{ij}>$. The configuration

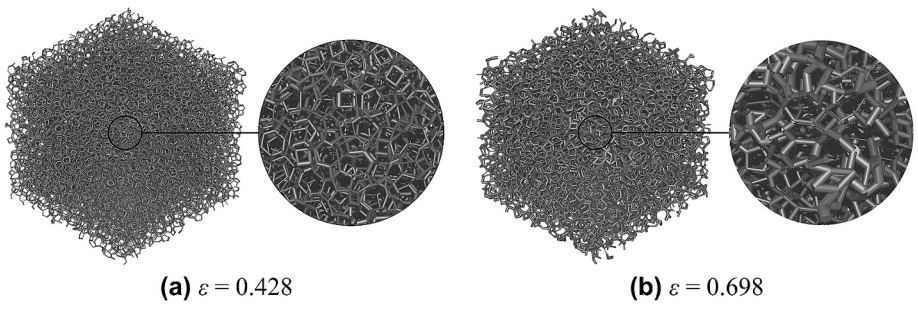

Fig. 13. Pore networks in packed beds at two representative porosities.

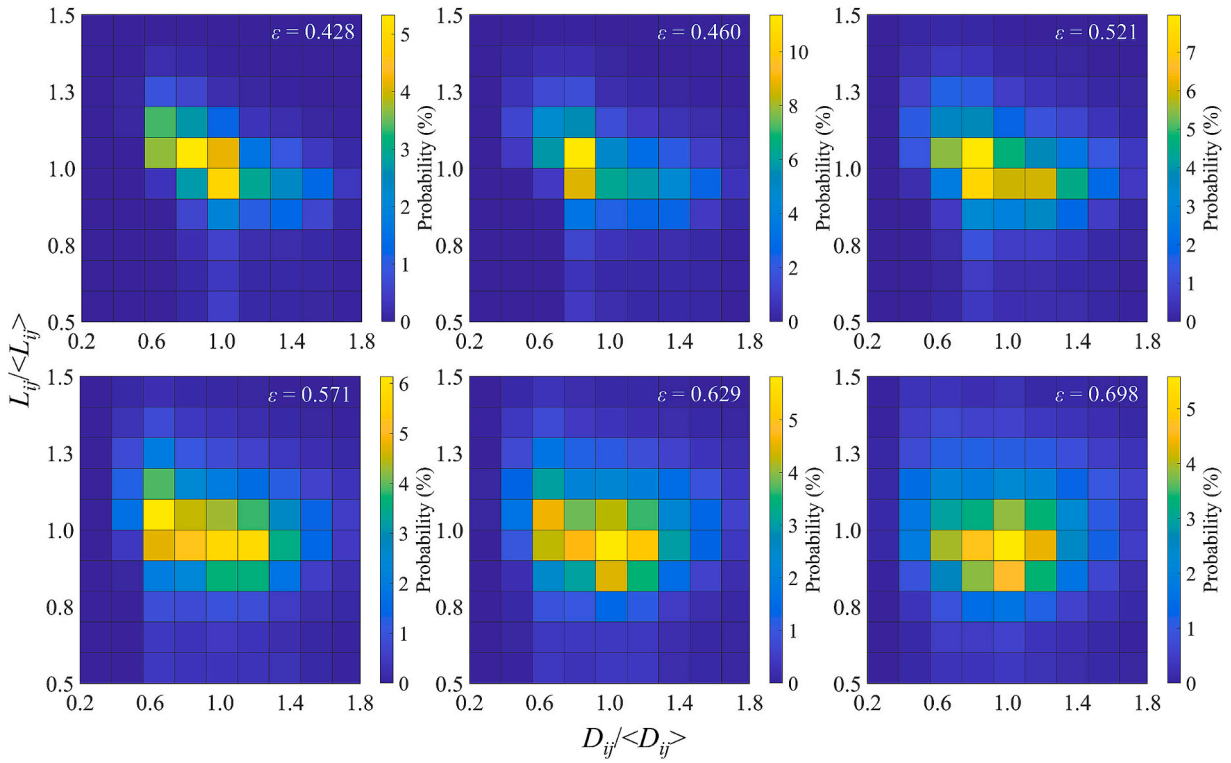

Fig. 14. Joint distribution of normalized throat diameter $D_{ij}/<D_{ij}>$ and normalized throat length $L_{ij}/<L_{ij}>$ in packed beds with varying porosity.

of pore connections and the dimensions of pore throats exhibit significant variation with changes in bed porosity. Typically, beds with higher porosity levels feature a greater number of larger-sized pore throats, reducing the system's structural uniformity. This trend underscores the critical influence of bed porosity on the organization and dimensions of the pore network, which, in turn, affects the fluid flow and heat transfer processes.

Fig. 14 provides a detailed representation of the joint distributions of normalized throat diameter $D_{ij}/<D_{ij}>$ and normalized throat length $L_{ij}/<L_{ij}>$ for packed beds with varying porosity levels. It is evident from the figure that the distribution becomes more focused for beds with lower porosity, signifying a more uniform pore structure within these beds. Conversely, the distributions are more dispersed at higher porosities, indicating a broader variability in pore sizes and shapes. This dispersion suggests the presence of a more heterogeneous pore structure, encompassing a wider range of sizes and configurations.

Pore-pore heat advection, which involves the transfer of mass and energy between adjacent pores, is significantly influenced by the structure of the pore network. Understanding this phenomenon is crucial for comprehending the dynamics of heat and mass flow within porous media. Fig. 15(a) delineates the correlation between the average advective heat transfer rate $<\mu_{ij}>$ and bed porosity at a gas velocity is 1.0 m/s and a gas temperature T_g is 100 °C. It is observed that the average advective heat transfer rate escalates with an increase in bed porosity, indicating that a more loosely structured bed facilitates enhanced mass-energy transfer through the pore spaces. Further insights are provided by Fig. 15(b), which illustrates the distribution of pore–pore advective heat μ_{ij} across particle beds of varying porosities. Notably, in beds with higher porosity, the peak of the distribution slightly shifts towards the left, while the tail of the distribution extends further into higher μ_{ij} values. This pattern suggests that compared to densely packed beds, those with a looser structure contain fewer

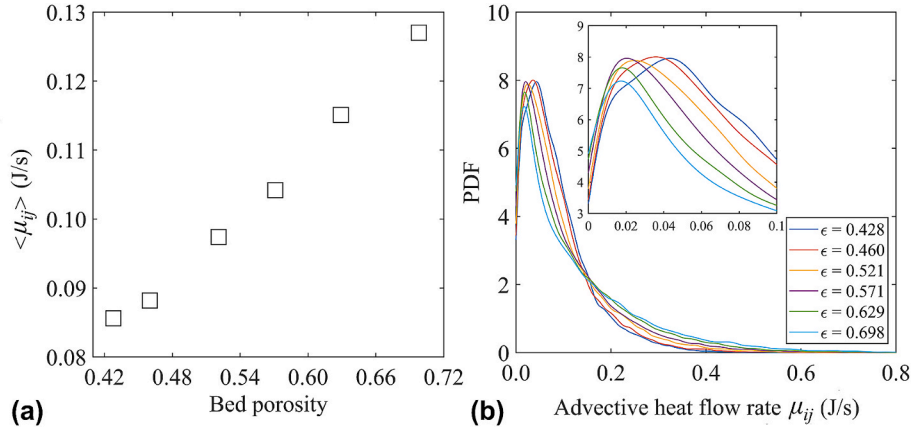

Fig. 15. (a) Relationship between average advective heat transfer rate $<\mu_{ij}>$ and bed porosity; (b) Distribution of advective heat transfer rate μ_{ij} for particle beds with varying porosities at a gas velocity of 1.0 m/s and gas temperature of 100 °C.

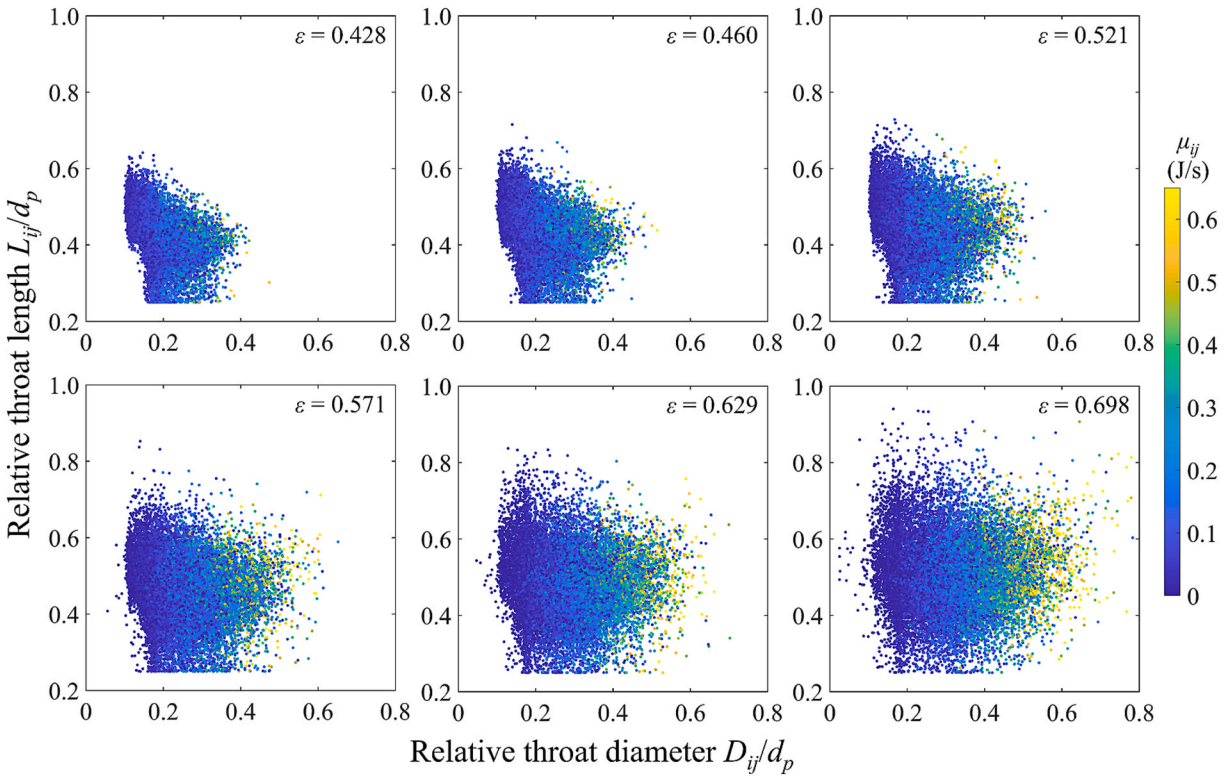

Fig. 16. Joint Influence of relative throat diameter D_{ij}/d_p and relative throat length L_{ij}/d_p on pore–pore advective heat transfer rates μ_{ij} for particle beds with varying porosities at a gas velocity of 1.0 m/s and a gas temperature of 100 °C.

regularly structured pores and a greater number of large, irregularly shaped pores. Such configurations can lead to localized spikes in volumetric flow rates and advective heat transfer rates, potentially resulting in uneven heat distribution during the transfer process.

To delve deeper into the relationship between throat geometry and its impact on advective heat transfer rate, Fig. 16 analyses the combined effects of throat diameter D_{ij} and throat length L_{ij} on the advective heat transfer rate μ_{ij} across particle beds of varying porosity. The figure illustrates that the influences of throat diameter and length are notably more dispersed in loosely packed beds, indicating that beds with higher porosity are predisposed to possessing pore throats that facilitate higher advective heat transfer rates. Larger throat diameters strongly correlate with higher advective heat transfer rates. This result suggests that throats with larger diameters are more conducive to increased mass-energy transfer. Conversely, throat length appears to exhibit no discernible correlation with the advective heat transfer rate, highlighting that the diameter of the throat is the predominant geometrical factor influencing pore-scale mass-energy flow. This phenomenon underlines the fact that loosely packed beds, characterized by a larger number of pore throats with substantial diameters, are capable of achieving higher heat transfer rates. Such structural attributes enhance the efficiency of advective heat transfer within the bed, underscoring the critical role of throat geometry in dictating the dynamics of heat and mass exchange at the pore scale.

In this work, the relative pore size is used to quantitatively characterize the dimensions of individual pores within the particle beds. This metric is defined as the ratio of the effective pore diameter to the particle diameter, denoted as d^*/d_p. The effective pore diameter is derived from the pore volume V: $d^* = 2\sqrt[3]{3V/4\pi}$, facilitating a standardized comparison across different beds. Fig. 17 illustrates the distribution of relative pore sizes across particle beds with varying porosity levels. Beds with denser packing exhibit a pronounced and concentrated peak at smaller relative pore sizes. In contrast, beds with looser packing display a broader and less defined peak at larger relative pore sizes. These

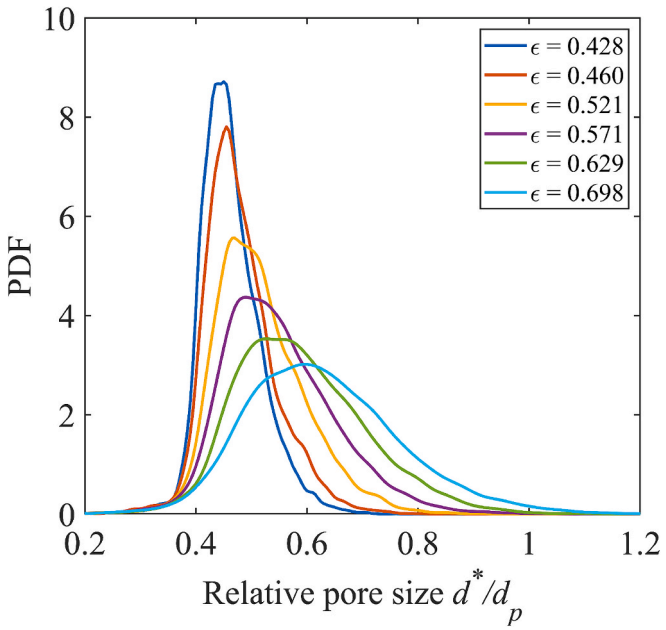

Fig. 17. Distributions of relative pore size d^*/d_p in particle beds with varying porosities.

distribution patterns indicate that denser packings tend to have a more uniform pore size distribution, whereas pores in looser packings are likely to be more irregular in shape. This observation aligns with the distributions of throat diameters and lengths in Fig. 14, further underscoring the correlation between bed porosity, pore size uniformity, and throat geometry.

As discussed, particle-pore heat convection plays a pivotal role in the

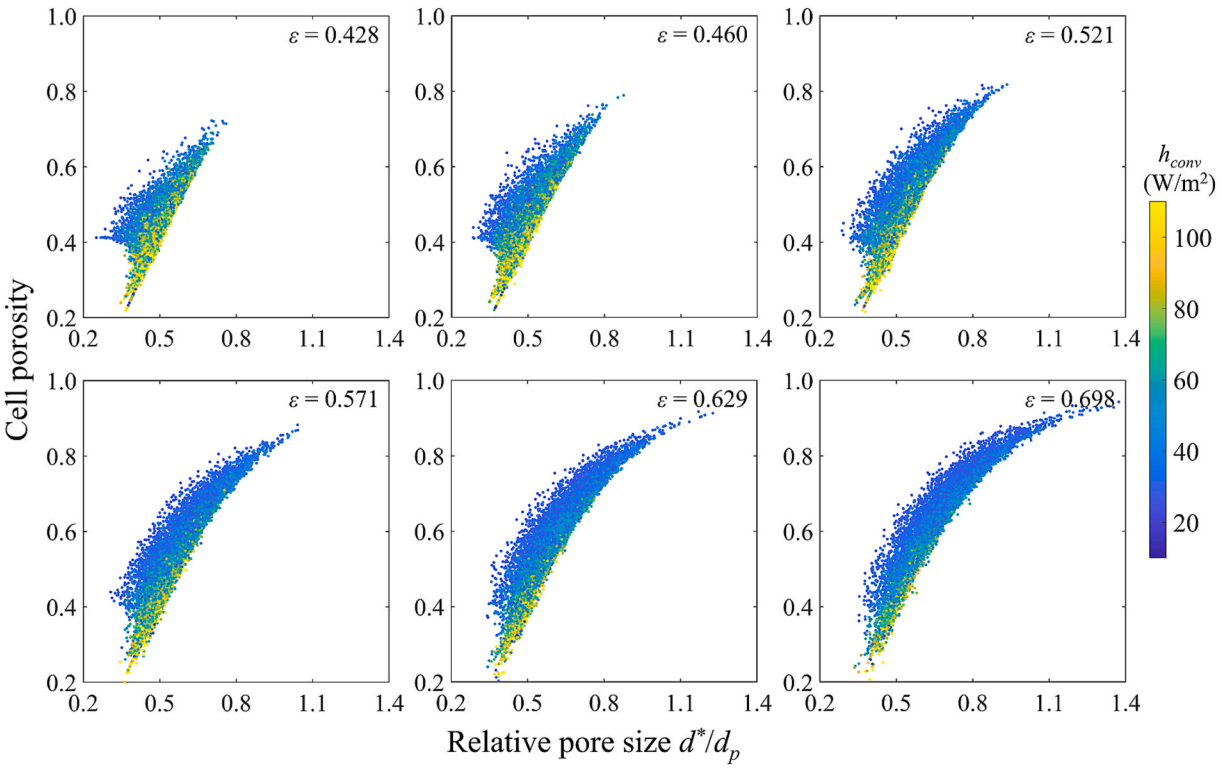

Fig. 18. Joint Influence of relative pore size d^*/d_p and cell porosity on pore scale convective heat transfer coefficient h_{conv} for particle beds in with varying porosities at a gas velocity of 1.0 m/s and gas temperature of 100 °C.

heat transfer process, especially at high fluid flow rates. Therefore, the specific impact of individual pore geometries on surrounding particles' convective heat transfer characteristics is examined, as shown in Fig. 18. The results reveal the combined influence of relative pore size d^*/d_p and cell porosity on the pore-scale convective heat transfer coefficient h_{conv} across particle beds of varying porosity where the gas velocity is 1.0 m/s and the gas temperature T_g is 100 °C. Here, the h_{conv} for a singular pore is defined as the aggregate of the partial heat transfer coefficients of the four adjacent particles comprising the pore unit. Cell porosity is quantified as the ratio between the volume of void space and the volume of the corresponding Delaunay cell. Also, a notable observation from this analysis is the presence of an 'invisible limit line' across different pore sizes, delineating the minimum porosity threshold inherent to a pore's geometric characteristics. Pores with regular geometries, such as a regular tetrahedron typically exemplify this threshold. Pores approximating this shape, or those proximal to the 'invisible limit line', manifest higher h_{conv} values. This phenomenon indicates that pores with near-regular shapes, such as smaller pores approximately 0.5 times the particle size, typically found in cells with porosities below 0.4, are more efficient in facilitating convective heat transfer. Consequently, dense packings, which are less prone to the formation of distorted pore shapes, exhibit a higher proportion of pores with elevated h_{conv}. In contrast, the heterogeneity in pore shapes within loosely packed structures results in a considerable number of pores exhibiting lower h_{conv} values.

4. Conclusion

This study introduces a novel PNM-based model to capture the complex interactions of conduction, convection, and radiation across varying packed bed porosities. By correlating pore geometry with localized heat transfer mechanisms, the model also provides insights into how structural features govern thermal behaviour at the pore scale. The following conclusions can be drawn:

(1) The model incorporates conduction, convection, and radiation heat transfer at a particle-pore scale, thereby providing insights into the impact of variations in bed porosity and pore structure on heat transfer properties. The accuracy of the PNM model for simulating heat transfer was validated against experimental data involving the cooling of hot spheres in a packed bed. Simulated temperature profiles and derived heat transfer coefficients closely matched experimental results. Further comparison between two radiation models revealed that the particle-pore scale approach more effectively accounts for structural heterogeneity in radiative heat transfer, especially at elevated temperatures.

(2) The overall heat transfer behavior within packed beds is strongly influenced by bed porosity, gas velocity, and temperature. Results reveals that higher gas velocities significantly accelerate heating, especially in low-porosity beds where increased interstitial velocities and specific interfacial areas enhance convective transfer. While conduction plays a notable role at low gas velocities and in denser beds, convection dominates at higher velocities. Radiative heat transfer is generally negligible at low temperatures but becomes increasingly important at elevated temperatures, surpassing conduction at high temperature.

(3) At the pore scale, the local structure of the pore network exerts a profound influence on the heat transfer behaviour. Denser beds exhibit more uniform and regularly shaped pore throats, while higher porosity leads to greater heterogeneity in throat geometry and pore size. This structural variability enhances the potential for localized high advective heat transfer, as larger throat diameters strongly correlate with increased mass-energy transport. Furthermore, pore-scale convective heat transfer is closely tied to pore geometry: pores with near-regular shapes, typically found in denser beds, exhibit higher local convective heat transfer coefficients.

This study highlights the complexities of heat transfer within particle

beds and establishes a foundation for exploring how bed porosity and local pore-scale variations influence thermal behaviour under diverse operating and material conditions. The developed framework is versatile and can be extended to a wide range of granular systems, including those involving non-spherical particles, dynamic packing, or reactive flows. It also holds potential as a practical tool for design optimization in particulate-based processes. Future work will aim to enhance the model's applicability by incorporating particle size and shape irregularities, dynamic flow conditions, and multi-physics coupling such as chemical reactions or phase change.

CRediT authorship contribution statement

Yi Zou: Writing – original draft, Conceptualization, Investigation, Methodology. **Shibo Kuang:** Writing – review & editing, Supervision, Conceptualization, Investigation. **Yongli Wu:** Methodology, Writing – review & editing. **Aibing Yu:** Supervision, Investigation, Writing – review & editing, Conceptualization.

Declaration of competing interest

The authors declare that they have no known competing financial interests or personal relationships that could have appeared to influence the work reported in this paper.

Acknowledgements

The authors are grateful to the ARC Research Hub for Smart Process Design and Control (IH230100010), the National Natural Science Foundation of China (No. 52034003 & No. 52006035), and the Natural Science Foundation of Jiangsu Province (No. BK20200269) for the financial support and the Australia National Computational Infrastructure for providing computing facilities.

Appendix A. Experimental setup for validation: Cooling of a hot sphere

As illustrated in F ig. A1, the experimental setup by Collier [45] consisted of a bed housed in a vertical cylindrical column. An air distributor was positioned at the bottom of the tube. A phosphor-bronze sphere was introduced into the bed for the cooling experiments. A radial hole was drilled into the sphere to accommodate the tip of a thermocouple, which was brazed in place. This thermocouple was connected to a digital temperature display and a chart recorder, enabling continuous monitoring of the sphere's temperature. The experimental procedure involved heating the bronze sphere in a Bunsen burner flame until it reached the desired temperature, after which it was rapidly inserted into the bed. The cooling process was then recorded via the thermocouple.

The specific experimental case used for comparison in this study was conducted at a gas velocity of $U = 0.58\ U_{mf}$ (0.429 m/s), using a 2 mm diameter hot bronze sphere. To replicate the experimental conditions in the numerical simulations, the same particle material properties, and gas velocity reported in the experiment were adopted, as summarized in Table 1. To reduce computational cost, a pseudo-2D "slot" packed bed was used, employing periodic boundary conditions along the front and rear sides of the domain, following similar approaches reported in the literature [43,44]. The gas was introduced at the bottom of the bed, in accordance with the experimental configuration. Since the original experiment did not specify the exact location of the bronze sphere, nine distinct positions within the simulated bed were selected to place the hot sphere. This strategy was intended to capture a broader range of temperature evolution profiles and improve the robustness of the validation. The temperature evolution of the sphere was directly recorded in the simulation for comparison with the experimental data.

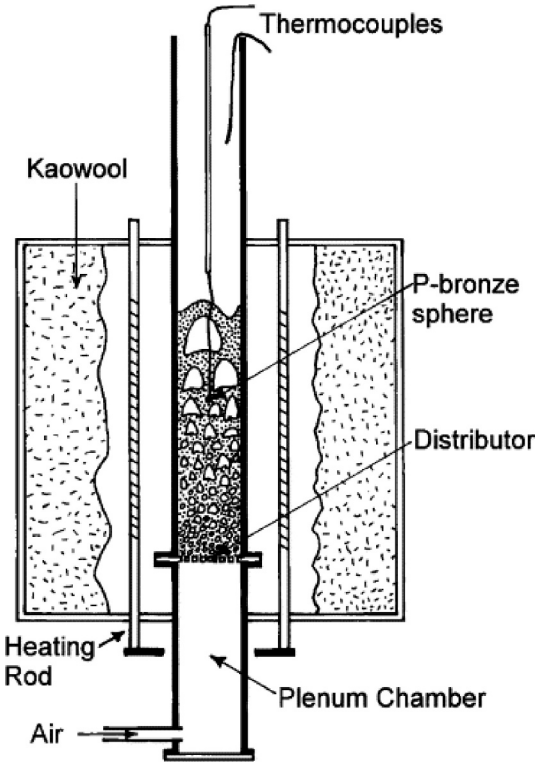

Fig. A1. Experiment setup for cooling of hot bronze sphere [45].

Data availability

Data will be made available on request.

References

[1] S. Kuang, Z. Li, A. Yu, Review on Modeling and simulation of Blast Furnace, Steel Res. Int. 89 (2018) 1700071.
[2] H.L. George, R.J. Longbottom, S.J. Chew, B.J. Monaghan, Flow of Molten Slag through a Coke Packed Bed, ISIJ Int. 54 (2014) 820–826.
[3] A.K. Ismail, N.H. Ibrahim, K.A. Shamsuddin, M.Z. Abdullah, M. Zubair, A practical approach in porous medium combustion for domestic application: a review, IOP Conference Series. 370 (2018) 012004.
[4] A. Blaszczuk, S. Jagodzik, Evaluation of heat transfer conditions during polydisperse gas–solid flow in an industrial fluidised bed reactor, Appl. Therm. Eng. 254 (2024) 123908.
[5] W. Dai, D. Hanaor, Y. Gan, The effects of packing structure on the effective thermal conductivity of granular media: a grain scale investigation, Int. J. Therm. Sci. 142 (2019) 266–279.
[6] V. Prasad, K. Brown, Q. Tian, Flow visualization and heat transfer experiments in fluid-superposed packed beds heated from below, Exp. Therm Fluid Sci. 4 (1991) 12–24.
[7] B.V. Perepelitsa, Experimental investigation of local heat transfer in the packing with triangular channels, Thermophys. Aeromech. 13 (2006) 549–555.
[8] G.C. Lindauer, Heat transfer in packed and fluidized beds by the method of cyclic temperature variations, AIChE J 13 (1967) 1181–1187.
[9] F. Zanotti, R.G. Carbonell, Development of Transport Equations for Multiphase Systems—III: Application to heat transfer in packed beds, Chem. Eng. Sci. 39 (1984) 299–311.
[10] Q. Xiong, T.G. Baychev, A.P. Jivkov, Review of pore network modelling of porous media: Experimental characterisations, network constructions and applications to reactive transport, J. Contam. Hydrol. 192 (2016) 101–117.
[11] P. Lovreglio, S. Das, K.A. Buist, E.A.J.F. Peters, L. Pel, J.A.M. Kuipers, Experimental and numerical investigation of structure and hydrodynamics in packed beds of spherical particles, AIChE J 64 (2018) 1896–1907.
[12] M. Nijemeisland, A.G. Dixon, CFD study of fluid flow and wall heat transfer in a fixed bed of spheres, AIChE J 50 (2004) 906–921.
[13] Y. Guo, J.S. Curtis, Discrete Element Method Simulations for complex Granular Flows, Annu. Rev. Fluid Mech. 47 (2015) 21–46.
[14] H.P. Zhu, Z.Y. Zhou, R.Y. Yang, A.B. Yu, Discrete particle simulation of particulate systems: a review of major applications and findings, Chem. Eng. Sci. 63 (2008) 5728–5770.
[15] H. Wu, N. Gui, X. Yang, J. Tu, S. Jiang, Numerical simulation of heat transfer in packed pebble beds: CFD-DEM coupled with particle thermal radiation, Int. J. Heat Mass Transf. 110 (2017) 393–405.
[16] P. Kumar, S.K. Saha, A. Sharma, Experimental and CFD-DEM study on local packing distribution and thermofluidic analysis of binary packed bed, Chem. Eng. Sci. 282 (2023) 119372.
[17] S. Bale, S. Tiwari, M. Sathe, A.S. Berrouk, K. Nandakumar, J. Joshi, Direct numerical simulation study of end effects and D/d ratio on mass transfer in packed beds, Int. J. Heat Mass Transf. 127 (2018) 234–244.
[18] Y.N. Chilamkurti, R.D. Gould, CFD-DEM and PR-DNS studies of low-temperature densely packed beds, Int. J. Heat Mass Transf. 159 (2020) 120056.
[19] S.T. Pham, B. Chareyre, E. Tsotsas, A. Kharaghani, Pore network modeling of phase distribution and capillary force evolution during slow drying of particle aggregates, Powder Technol. 407 (2022) 117627.
[20] K.E. Thompson, H.S. Fogler, Modeling flow in disordered packed beds from pore-scale fluid mechanics, AIChE J 43 (1997) 1377–1389.
[21] I. Fatt, The network model of porous media, Trans. AIME 207 (1956) 144–181.
[22] M.J. Blunt, Flow in porous media — pore-network models and multiphase flow, Curr. Opin. Colloid Interface Sci. 6 (2001) 197–207.
[23] I. Tomac, M. Gutierrez, Formulation and implementation of coupled forced heat convection and heat conduction in DEM, Acta Geotech. 10 (2015) 421–433.
[24] G.J. Cheng, A.B. Yu, P. Zulli, Evaluation of effective thermal conductivity from the structure of a packed bed, Chem. Eng. Sci. 54 (1999) 4199–4209.
[25] P. Chen, K. Huang, F. Wang, W. Xie, S. Wei, D. Yang, Simulation of heat and mass transfer in a grain pile on the basis of a 2D irregular pore network, Fluid Dynamics Materials Proc 15 (2019) 367–389.
[26] G. Cheng, J. Gan, D. Xu, A. Yu, Evaluation of effective thermal conductivity in random packed bed: Heat transfer through fluid voids and effect of packing structure, Powder Technol. 361 (2020) 326–336.
[27] R. Caulk, L. Scholtès, M. Krzaczek, B. Chareyre, A pore-scale thermo–hydro-mechanical model for particulate systems, Comput. Methods Appl. Mech. Eng. 372 (2020) 113292.
[28] T. Morimoto, C. O'Sullivan, D.M.G. Taborda, Capturing particle-fluid heat transfer in thermo-hydro-mechanical analyses using DEM coupled with a pore network model, Powder Technol. 429 (2023) 118944.
[29] N. Govender, P.W. Cleary, M. Kiani-Oshtorjani, D.N. Wilke, C.-Y. Wu, H. Kureck, The effect of particle shape on the packed bed effective thermal conductivity based on DEM with polyhedral particles on the GPU, Chem. Eng. Sci. 219 (2020) 115584.
[30] S.J. Rodrigues, N. Kazemi, E. Tsotsas, Local-scale variability in packed beds of polyhedral particles: Structural and thermal distribution, Powder Technol. 451 (2025) 120461.
[31] G.J. Cheng, A.B. Yu, particle scale evaluation of the effective thermal conductivity from the structure of a packed bed: radiation heat transfer, Ind. Eng. Chem. Res. 52 (2013) 12202–12211.
[32] P.A. Cundall, O.D. Strack, A discrete numerical model for granular assemblies, Géotechnique 29 (1979) 47–65.
[33] H.P. Zhu, Z.Y. Zhou, R.Y. Yang, A.B. Yu, Discrete particle simulation of particulate systems: theoretical developments, Chem. Eng. Sci. 62 (2007) 3378–3396.
[34] S. Ergun, A.A. Orning, Fluid Flow through Randomly Packed Columns and Fluidized Beds, Ind. Eng. Chem. 41 (1949) 1179–1184.
[35] Z.Y. Zhou, A.B. Yu, P. Zulli, Particle scale study of heat transfer in packed and bubbling fluidized beds, AIChE J 55 (2009) 868–884.
[36] G.K. Batchelor, Apos, R.W. Brien, Thermal or electrical conduction through a granular material, Proc. Royal Soc. Lond. Math. Phys Sci. 355 (1997) 313–333.
[37] W.J. Yang, Z.Y. Zhou, A.B. Yu, Particle scale studies of heat transfer in a moving bed, Powder Technol. 281 (2015) 99–111.
[38] Q. Hou, D. E, S. Kuang, A. Yu, A process scaling approach for CFD-DEM modelling of thermochemical behaviours in moving bed reactors, Fuel Process. Technol. 202 (2020) 106369.
[39] L.R. Jones, Diffuse radiation view factors between two spheres, J. Heat Transfer 87 (1965) 421–422.
[40] D.J. Gunn, Transfer of heat or mass to particles in fixed and fluidised beds, Int. J. Heat Mass Transf. 21 (1978) 467–476.
[41] Y. Wu, Q. Hou, Z. Qi, A. Yu, Particle–pore scale modelling of particle–fluid flows, Chem. Eng. Sci. 235 (2021) 116500.
[42] Y. Wu, Q. Hou, A. Yu, Pore-scale study of fluid flow and drag force in randomly packed beds of different porosities, Ind. Eng. Chem. Res. 58 (2019) 5041–5053.
[43] G. Wei, H. Zhang, X. An, B. Xiong, S. Jiang, CFD-DEM study on heat transfer characteristics and microstructure of the blast furnace raceway with ellipsoidal particles, Powder Technol. 346 (2019) 350–362.
[44] D. E, P. Zhou, S. Guo, J. Zeng, J. Cui, Y. Jiang, Y. Lu, Z. Jiang, Z. Li, S. Kuang, Particle shape effect on hydrodynamics and heat transfer in spouted bed: a CFD–DEM study, Particuology 69 (2022) 10–21.
[45] A.P. Collier, A.N. Hayhurst, J.L. Richardson, S.A. Scott, The heat transfer coefficient between a particle and a bed (packed or fluidised) of much larger particles, Chem. Eng. Sci. 59 (2004) 4613–4620.